Defect and dopant properties in $CaMnO_3$

Cite as: AIP Advances **11**, 055106 (2021); https://doi.org/10.1063/5.0048401
Submitted: 22 February 2021 . Accepted: 19 April 2021 . Published Online: 03 May 2021

Navaratnarajah Kuganathan, and Alexander Chroneos

Defect and dopant properties in $CaMnO_3$

Cite as: AIP Advances 11, 055106 (2021); doi: 10.1063/5.0048401
Submitted: 22 February 2021 • Accepted: 19 April 2021 •
Published Online: 3 May 2021

Navaratnarajah Kuganathan[1,2,a] and Alexander Chroneos[1,2]

AFFILIATIONS

[1] Department of Materials, Imperial College London, London SW7 2AZ, United Kingdom
[2] Faculty of Engineering, Environment and Computing, Coventry University, Priory Street, Coventry CV15FB, United Kingdom

[a] Author to whom correspondence should be addressed: n.kuganathan@imperial.ac.uk

ABSTRACT

$CaMnO_3$-based ceramics have been the subject of considerable research due to their potential application in solid oxide fuel cells, thermoelectric generators, and catalysis. The computational modeling technique based on the classical pair-wise potentials has allowed atomic-scale insights into the defect chemistry, diffusion of Ca^{2+} and O^{2-} ions, and solution of various dopants in this material. The Ca/Mn anti-site was found to be the most favorable intrinsic defect suggesting disorder, which would be sensitive to synthesis conditions. The second most favorable disorder in $CaMnO_3$ involves loss of CaO, resulting in calcium and oxygen vacancies, which in turn can promote vacancy mediated self-diffusion. The activation energy for oxygen migration (1.25 eV) is much lower than that for calcium (4.42 eV). Favorable isovalent dopants on the Ca and Mn sites were found to be Fe^{2+} and Ge^{4+}, respectively. The formation of O vacancies can be facilitated by doping of single dopants Fe^{2+} and Al^{3+} on the Mn site. Dual dopants Ni–Fe and Al–Ga on the Mn site can also facilitate the introduction of oxygen vacancies required for the vacancy assisted oxygen diffusion.

I. INTRODUCTION

Perovskite-type oxides (ABO_3) have become a material of increasing scientific interest in recent years as they exhibit a wide range of useful properties including thermoelectric, magnetic, and catalytic properties.[1–5] One of the key features of perovskites is that their structures are extremely flexible over metal-ion doping on either the A or the B site, maintaining their perovskite-type framework. The desired applications of these materials have been achieved by tailoring the A/B/O compositions mainly via substitutional doping.[6–9] The oxygen ion conductivities of these materials in both stoichiometric and non-stoichiometric forms have been studied well as the performance of advanced energy technologies such as solid oxide fuel cells is mainly dependent on the diffusion of oxygen ions.[10–12]

Perovskite-type $CaMnO_3$ is one of the promising oxide materials that have found applications in several technologically relevant areas such as catalysis and power generation.[13–15] A significant effort has been made on the development of this material for use in thermoelectric power generators, electrocatalysis, and Li-ion batteries.[16–22] The thermoelectric properties of this material and its modified form have been previously investigated.[1,23–26] An experimental study by Kabir *et al.*[25] shows that the doping of W in $CaMnO_3$ enhances its thermoelectric properties. Another experimental study indicates that Bi doping at low concentration can improve its thermoelectric properties.[23] A combined experimental and computational study shows that Sr–Mo doped $CaMnO_3$ exhibits enhanced thermoelectric properties.[26] Nonstoichiometric $CaMnO_{3-\delta}$ has been determined to be an inexpensive and active bifunctional catalytic material in oxygen reduction and oxygen evolution reactions for oxygen-based electrochemical technologies.[14] Stability and efficiency of Li-ion storage have been studied recently by Chang *et al.*,[22] and it was concluded that the $CaMnO_3$ anode exhibits an excellent cycle-performance with long-life and high rate capacity at different temperatures.

Intrinsic and extrinsic defect properties are of great importance as they directly or indirectly govern the physical properties of a material. Information about intrinsic defects, promising dopants, and diffusion of ions is crucial as it can help tailor the material properties for its improvement. In this respect, atomistic scale simulation based on the classical potentials is an efficient tool to study the intrinsic and extrinsic defect properties.[27,28] This methodology has been applied to various oxide materials including batteries and solid oxide fuel cell materials.[29–34] In this study, we examine the

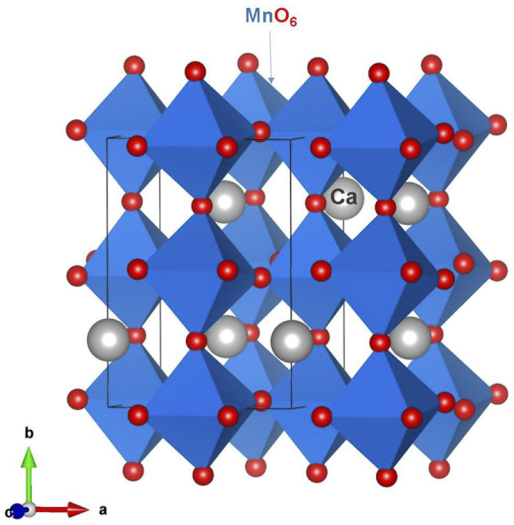

FIG. 1. Crystal structure of bulk $CaMnO_3$.

defect properties, kinetics of Ca^{2+} and O^{2-} ions, and solution of various mono- and bi-dopants in $CaMnO_3$ with the aid of atomistic simulation techniques based on the classical pair potentials.

II. COMPUTATIONAL METHODS

We performed static atomistic simulations based on the classical pair potentials as implemented in the generalized utility lattice program (GULP).[35] In this method, ionic interactions are described in the form of long-range (Coulombic) and short-range (electron–electron repulsion and van-der Waals attraction) interactions. Short range forces were modeled using Buckingham potentials. Full geometry optimizations were performed using the Broyden–Fletcher–Goldfarb–Shanno (BFGS) algorithm.[36] In all relaxed configurations, forces on the atoms were smaller than 0.001 eV/Å. The Mott–Littleton method[37] was used to model point defects and migrating ions. In this method, two spherical regions are defined, with atoms in the inner spherical region being relaxed explicitly. In the outer spherical region, atoms are treated using approximate quasi-continuum methods, and forces on the atoms in this region are relatively weak. Vacancy mediated Ca ion diffusion was calculated considering seven interstitial Ca ions between local Ca hops. Activation energy was defined as the local maximum energy along the diffusion path. A similar methodology has been used to calculate the O ion diffusion pathways and their corresponding activation energies in many oxide materials.[38–40] The present calculation is based on the full ionic charge model within the dilute limit. Therefore, the defect energies will be overestimated; however, the relative energies and the trends will be consistent.[29]

TABLE II. Calculated and experimental lattice parameters of cubic $CaMnO_3$.

Parameter	Calculated	Experiment[41]	$\|\Delta\|$ (%)
a (Å)	5.314	5.279	0.66
b (Å)	7.508	7.448	0.80
c (Å)	5.306	5.264	0.80
$\alpha = \beta = \gamma$ (deg)	90.0	90.0	0.00
V $(Å)^3$	211.68	206.97	2.28

III. CRYSTAL STRUCTURES OF $CaMnO_3$

$CaMnO_3$ crystallizes in the orthorhombic perovskite phase with the space group of *Pnma*(no. 62).[41] Experimental lattice parameters reported by Poeppelmeier *et al.*[41] are a = 5.279 Å, b = 7.448 Å, c = 5.264 Å, and $\alpha = \beta = \gamma = 90°$. In the crystal structure, there are corner sharing MnO_6 octahedral units with a three dimensional network, as shown in Fig. 1. The calcium ions are in a twelve-coordination environment occupying the body centered positions of the crystal. The crystal structure of $CaMnO_3$ was relaxed under constant pressure to determine the equilibrium lattice constants and validate the Buckingham potentials used in this study[42–44] (see Table I).The calculated lattice parameters are in good agreement with corresponding experimental values, showing the efficacy of these potentials (refer to Table II).

IV. RESULTS AND DISCUSSION

A. Intrinsic defects

The intrinsic point defects (vacancies and interstitials) are of great importance as they influence the diffusion property of a material. Defect energies calculated in this study are expected to be overestimated as ions are considered as spherical shapes with full charge at the dilute limit. Defect parameters such as migration and formation energies can be defined by comparing the real (defective) crystal to an isobaric or isochoric ideal (non-defect) crystal. These sets of defect formation parameters are interconnected via thermodynamic relations.[45–47] Current calculations correspond to the isobaric parameters for migration and formation processes. Point defect energies are generally difficult to determine via experiments

TABLE I. Buckingham potential parameters used in this study.[42–44] Two-body $\Phi_{ij}(r_{ij}) = A_{ij}\exp(-r_{ij}/\rho_{ij}) - C_{ij}/r_{ij}^6$, where A, ρ, and C are parameters that were selected carefully to reproduce the experimental data. The values of Y and K represent the shell charges and spring constants, respectively.

Interaction	A (eV)	ρ (Å)	C (eV $Å^6$)	Y (e)	K/(eV $Å^{-2}$)
Ca^{2+}–O^{2-}	1 090.40	0.337 2	0.000	1.26	34.00
Mn^{4+}–O^{2-}	3 087.826	0.282 2	0.000	4.00	99 999
O^{2-}–O^{2-}	22 764.3000	0.149 000	27.879	−2.86	74.92

but can be accessed by theoretical modeling. Here, we first calculate the isolated point defect formation energies in order to give the Frenkel, Schottky, and anti-site disorder energies. The following reaction equations written using the Kröger–Vink notation[48] describe the Frenkel, Schottky, and anti-site disorder:

$$\text{Ca Frenkel}: \mathrm{Ca}_{\mathrm{Ca}}^{\mathrm{X}} \rightarrow V_{\mathrm{Ca}}'' + \mathrm{Ca}_{\mathrm{i}}^{\bullet\bullet}, \tag{1}$$

$$\text{Mn Frenkel}: \mathrm{Mn}_{\mathrm{Mn}}^{\mathrm{X}} \rightarrow V_{\mathrm{Mn}}'''' + \mathrm{Mn}_{\mathrm{i}}^{\bullet\bullet\bullet\bullet}, \tag{2}$$

$$\text{O Frenkel}: \mathrm{O}_{\mathrm{O}}^{\mathrm{X}} \rightarrow V_{\mathrm{O}}^{\bullet\bullet} + \mathrm{O}_{\mathrm{i}}'', \tag{3}$$

$$\text{Schottky}: \mathrm{Ca}_{\mathrm{Ca}}^{\mathrm{X}} + \mathrm{Mn}_{\mathrm{Mn}}^{\mathrm{X}} + 3\mathrm{O}_{\mathrm{O}}^{\mathrm{X}} \rightarrow V_{\mathrm{Ca}}'' + V_{\mathrm{Mn}}'''' + 3V_{\mathrm{O}}^{\bullet\bullet} + \mathrm{CaMnO_3}, \tag{4}$$

$$\text{CaO Schottky}: \mathrm{Ca}_{\mathrm{Ca}}^{\mathrm{X}} + \mathrm{O}_{\mathrm{O}}^{\mathrm{X}} \rightarrow V_{\mathrm{Ca}}'' + V_{\mathrm{O}}^{\bullet\bullet} + \mathrm{CaO}, \tag{5}$$

$$\mathrm{MnO_2}\ \text{Schottky}: \mathrm{Mn}_{\mathrm{Mn}}^{\mathrm{X}} + 2\mathrm{O}_{\mathrm{O}}^{\mathrm{X}} \rightarrow V_{\mathrm{Mn}}'''' + 2V_{\mathrm{O}}^{\bullet\bullet} + \mathrm{MnO_2}, \tag{6}$$

$$\text{Ca/Mn antisite (isolated)}: \mathrm{Ca}_{\mathrm{Ca}}^{\mathrm{X}} + \mathrm{Mn}_{\mathrm{Mn}}^{\mathrm{X}} \rightarrow \mathrm{Ca}_{\mathrm{Mn}}'' + \mathrm{Mn}_{\mathrm{Ca}}^{\bullet\bullet}, \tag{7}$$

$$\text{Ca/Mn antisite (cluster)}: \mathrm{Ca}_{\mathrm{Ca}}^{\mathrm{X}} + \mathrm{Mn}_{\mathrm{Mn}}^{\mathrm{X}} \rightarrow \{\mathrm{Ca}_{\mathrm{Mn}}'' : \mathrm{Mn}_{\mathrm{Ca}}^{\bullet\bullet}\}^{\mathrm{X}}, \tag{8}$$

$$\text{Binding energy (BE)}: E_{cluster} - E_{isolated}. \tag{9}$$

Examination of the defect reaction energies reported in Table III suggests that the formation energies of Frenkel disorder are relatively high although O-Frenkel is the lowest among other Frenkels, with a reaction energy of 5.59 eV. The highest formation energy of Mn Frenkel (12.23 eV) is partly due to the charge of the Mn^{4+} ion being higher than that of Ca^{2+}. Schottky-type disorder in this system is also relatively high (>4 eV), and therefore, it is unlikely that these defects will be present at significant concentration at room temperature. The most thermodynamically stable defect is found to be the Ca–Mn anti-site defect cluster in which both Mn and Ca positions are exchanged simultaneously (2.92 eV). In the isolated form, both Ca_{Mn}'' and $Mn_{Ca}^{\bullet\bullet}$ defects are present further apart in the crystal. The energy difference between the cluster form of anti-site defect and the isolated form of defect is defined as the binding energy. The calculated binding energy is −1.20 eV, inferring the preference of aggregating isolated defects forming a cluster $\{Ca_{Mn}'' : Mn_{Ca}^{\bullet\bullet}\}^{X}$. The anti-site defect has been found in many oxide materials experimentally and theoretically.[49–51]

TABLE III. Reaction energies for different defect processes.

Process	Equation	Reaction energy (eV)/defect
Ca Frenkel	1	6.72
Mn Frenkel	2	12.23
O Frenkel	3	5.59
Schottky	4	5.42
CaO-Schottky	5	4.29
MnO_2-Schottky	6	6.36
Ca–Mn anti-site (isolated)	7	4.12
Ca–Mn anti-site (cluster)	8	2.92
Binding energy	9	−1.20

B. Diffusion of Ca^{2+} and O^{2-} ions

Ionic transport is one of the important properties of a material to assess its ionic conductivity. It can be difficult to determine diffusion pathways and mechanisms experimentally. The present classical simulation method is appropriate to find various Ca and O ion diffusion pathways together with activation energies.

Diffusion of calcium ions in calcium based oxide materials is predicted to be slow due to double positive charge of the migrating Ca ion, which is strongly attracted by negatively charged oxygen ions in the lattice. Computational modeling based on density functional theory (DFT) and classical pair potentials shows that activation energies of Ca ion diffusion in Ca-bearing oxide materials are high, indicating the slow movement of Ca ions.[52,53]

For the Ca migration, three main local hops between adjacent Ca sites were identified (refer to Fig. 2). The lowest migration barrier is 4.42 eV (path A) (refer to Table IV). As this path alone cannot facilitate transport of Ca across the unit cell, local Ca hops (A–C) were connected to construct long-range Ca ion diffusion channels. The long-range Ca migration pathway (A ↔ A ↔ A ↔ A) with the lowest activation energy is calculated along the *b* axis with an activation energy of 4.42 eV. Energy profile diagrams for these hops are shown in Fig. 3. Similar activation energy (4.60 eV) is calculated for pyroxene based $CaMn(SiO_3)_2$ structure although this compound has a different crystallographic structure from $CaMnO_3$.[52] DFT simulation has been performed by Torres *et al.*[54] on different calcium

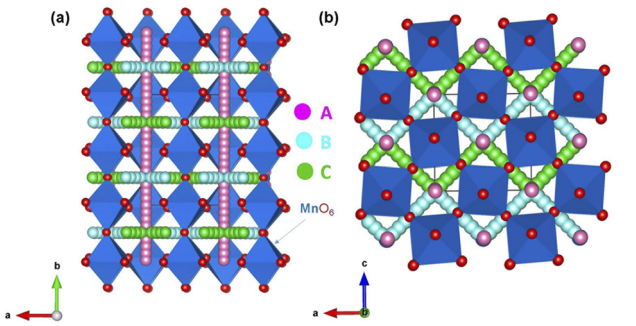

FIG. 2. Possible long-range Ca ion vacancy migration pathways shown in (a) *ab* and (b) *ac* planes.

TABLE IV. Ca–Ca distances and their corresponding activation energies for the Ca ion migration in $CaMnO_3$.

Migration path	Ca–Ca separation (Å)	Activation energy (eV)
A	3.754	4.42
B	3.749	4.45
C	3.759	4.44

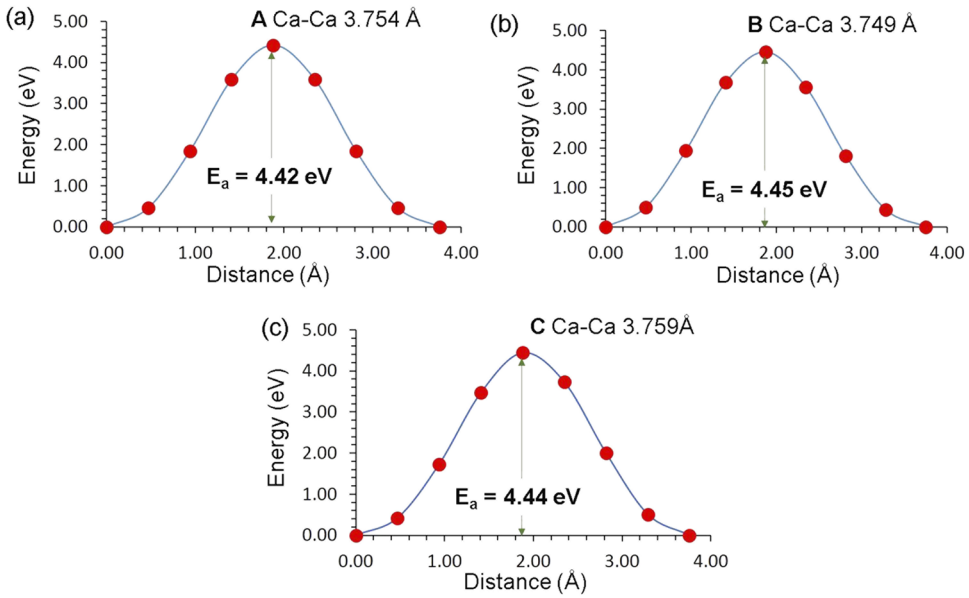

FIG. 3. Three different energy profiles (as shown in Fig. 2) of Ca vacancy hopping between the nearest neighbor Ca sites in $CaMnO_3$.

manganate based oxide structures. Activation energies calculated for Ca ions in $CaMn_2O_4$, $Ca_2Mn_2O_5$, and $CaMn_2O_4$ were reported to be 1.00, 2.60, and 2.20 eV, respectively.[54] Low activation energies can be due to the lower charge states of Mn and shorter Ca–Ca hopping distances than those found in $CaMnO_3$.

Next, we considered possible O vacancy hops between adjacent O ions in the lattice. Four possible migration hops [(P–S) in Fig. 4] led to three long-range O ion migration pathways (P ↔ P ↔ P ↔ P, Q ↔ Q ↔ Q ↔ Q, and R ↔ S ↔ R ↔ S). The activation energies for hops ranged between 1.25 and 5.12 eV (refer to Table V and Fig. 5). For the long-range pathways (P ↔ P ↔ P ↔ P) and (Q ↔ Q ↔ Q ↔ Q), as shown in Fig. 5, the activation energies were 1.25 and 1.99 eV respectively. The third long-range pathway (R ↔ S ↔ R ↔ S) consists of hops R and S, and these hops exhibit high activation energies of 4.24 and 5.12 eV, respectively. Thus, the overall activation energy for this pathway is 5.12 eV. The O^{2-} ions will preferably migrate along the *a* axis (P ↔ P ↔ P ↔ P) as this long range diffusion pathway exhibits the lowest overall migration energy of 1.25 eV. As activation energy calculated for long-range oxygen ion migration is considerably lower than that calculated for Ca ion migration, oxygen ion migration is faster than Ca ion migration in this material.

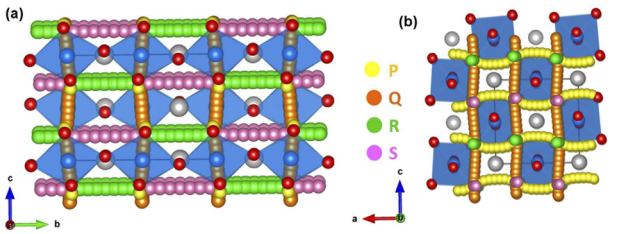

FIG. 4. Possible long-range O ion vacancy migration pathways shown in (a) *bc* and (b) *ac* planes.

TABLE V. O–O distances and their corresponding activation energies for the O ion migration in $CaMnO_3$.

Migration path	O–O separation (Å)	Activation energy (eV)
P	2.664	1.25
Q	2.679	1.99
R	3.434	4.24
S	4.069	5.12

C. Solution of dopants

Dopants play a significant role in tuning the properties of a material. Interstitial dopants generally introduce strain in the lattice. Substitutional dopants with different charge states and sizes compared to the atom to be substituted will also change the properties of the host material. Solution energies calculated using different appropriate charge compensation defects and lattice energies would provide valuable information about the promising dopants that can be tested experimentally. The oxygen vacancy formation in $CaMnO_3$ is one of the important processes that need to be addressed using appropriate dopants on the Mn site. Furthermore, isovalent dopants are also important in preventing phase transformation.

1. Divalent dopants

First, we considered some divalent dopants (M = Ni, Mg, Co, Fe, Sr, and Ba) on the Ca site. The following reaction equation was used to calculate the solution energy, and in this process, no charge compensating defects were necessary:

$$MO + Ca_{ca}^{X} \rightarrow M_{Ca}^{X} + CaO. \quad (10)$$

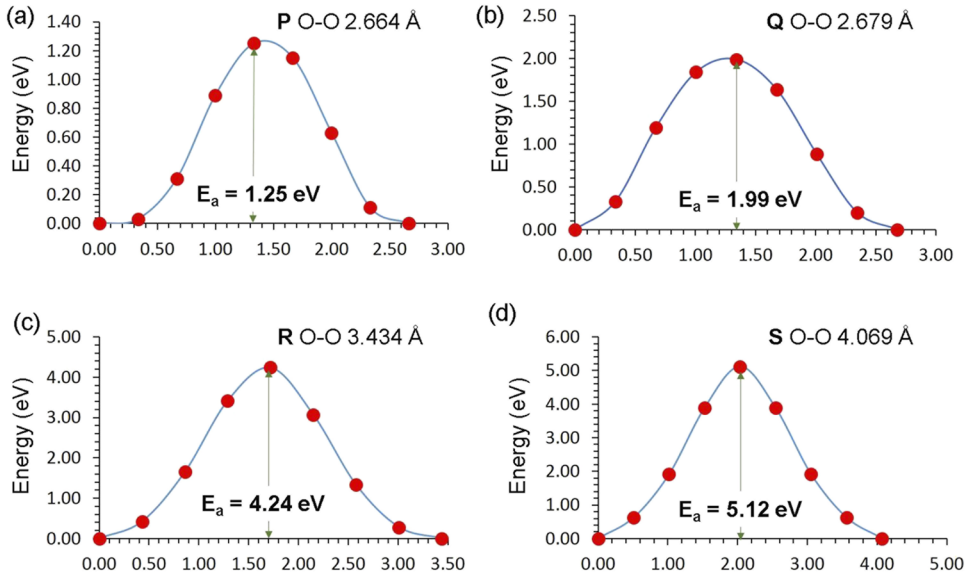

FIG. 5. Four different energy profiles (as shown in Fig. 4) of O vacancy hopping between the nearest neighbor O sites in $CaMnO_3$.

An exoergic solution energy of −0.55 eV was calculated for Fe^{2+} (refer to Fig. 6). This suggest that Fe^{2+} is the most favorable dopant, which can form a possible composition of $Ca_{1-x}Fe_xMnO_3$ ($0.0 < x < 1.0$) that can be synthesized experimentally. The second most favorable dopant is calculated to be Sr^{2+} with a solution energy of 0.20 eV, suggesting that this dopant could also be considered for doping. Bulfin *et al.*[55] performed an experimental study on $CaMnO_3$ and $Ca_{0.8}Sr_{0.2}MnO_3$ and observed redox properties better than those observed in $CaMnO_3$. High positive solution energies are calculated for other dopants, meaning that they are unlikely to be doped at normal temperatures. The preference of Fe^{2+} can be due to a close match between its ionic radius (0.92 Å) and the ionic radius of the Ca^{2+} ion (1.00 Å). The highest solution energy is observed for Ba^{2+} due to its larger ionic radius (1.42 Å) than Ca^{2+}.

Thereafter, we considered the divalent substitution on the Mn site. This process will introduce oxygen vacancies as charge compensating defects in the lattice [Eq. (11) below], making this material more conductive,

$$MO + Mn_{Mn}^{X} + O_{o}^{X} \rightarrow M_{Mn}'' + V_{O}^{\bullet\bullet} + MnO_2. \quad (11)$$

Solution energies were calculated considering two defects (M_{Mn}'' + $V_O^{\cdot\cdot}$): further apart (isolated) and close to each other (cluster). In all cases, solution energies calculated for clusters are found to be more energetically favorable than that calculated for isolated forms [refer to Fig. 7(a)]. The most favorable dopant for this process is Fe^{2+}. Solution energies calculated for Ni, Mg, and Co are close to each other and ~1 eV higher than the solution energy calculated for Fe. The larger ionic radii of Sr^{2+} and Ba^{2+} resulted in higher solution energies. Figure 7(b) presents the binding energies of divalent dopants with respect to their electronegativities. Binding energy increases as the electronegativity of the divalent dopant increases (except for Co and Ni).

Dual divalent dopants (M or R = Ni, Mg, Co, Fe, Sr, and Ba) were also considered on the Mn sites. As discussed earlier, this process will also introduce oxygen vacancies with double concentration, according to the following equation:

$$MO + RO + 2Mn_{Mn}^{X} + 2O_{o}^{X} \rightarrow M_{Mn}'' + R_{Mn}'' + 2V_{O}^{\bullet\bullet} + 2MnO_2. \quad (12)$$

Table VI reports the solution energies. Solution energies were calculated for this process in two different ways. Defects were considered as isolated and cluster forms. In the isolated forms, each defect energy was calculated independently. In the cluster form, all four defects were close to each other. The difference between these two solution energies is the binding energy. Solution energies are more favorable for the cluster form; the isolated form due to the preference of aggregation isolated defects forms clusters, as evidenced by the exoergic binding energies. The most favorable dual dopant is calculated to be Ni–Fe. Solution energies calculated for Co–Fe and Mg–Fe are higher only by 0.04 and 0.13 eV, respectively, than

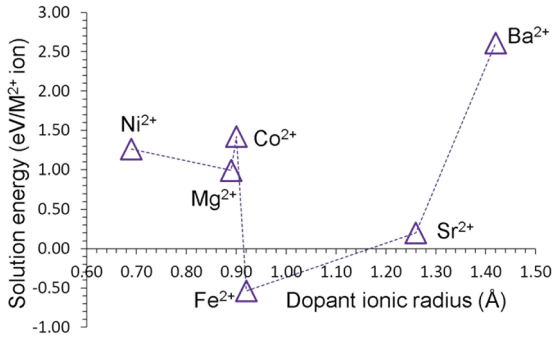

FIG. 6. Solution energy of MO (M = Ni, Mg, Co, Fe, Sr, and Ba) with respect to the M^{2+} ionic radius.

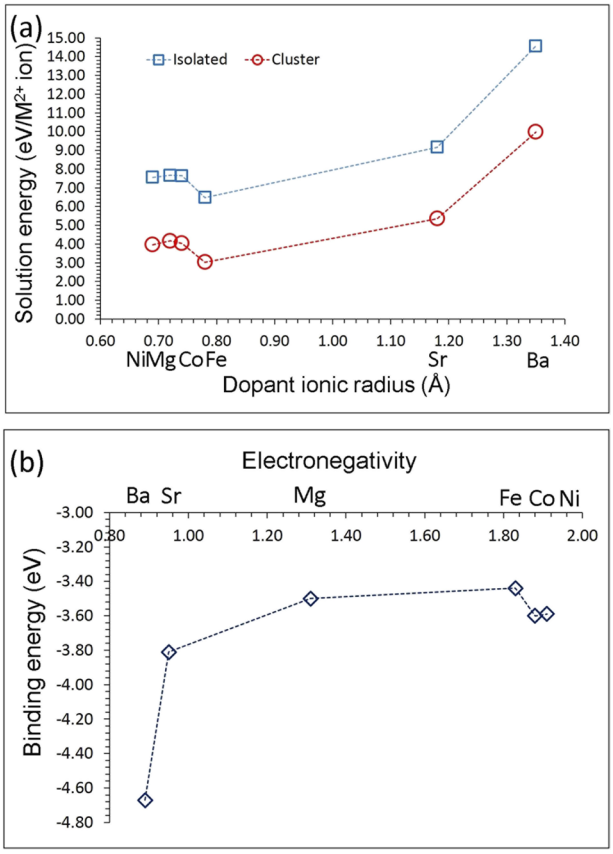

FIG. 7. (a) Solution energy of MO (M = Ni, Mg, Co, Fe, Sr, and Ba) with respect to the M^{2+} ionic radius and (b) binding energy of corresponding isolated defects forming a cluster with respect to electronegativity of the dopants.

TABLE VI. Solution energies calculated for dual-divalent dopants substituted on the Mn site.

Co-dopants	Solution energy (eV/dopant)		Binding energy (eV)
	Isolated	Cluster	
Ni–Mg	7.62	2.71	−4.91
Ni–Co	7.60	2.65	−4.95
Ni–Fe	7.02	2.13	−4.89
Ni–Sr	8.35	3.17	−5.19
Ni–Ba	11.10	5.15	−5.95
Mg–Co	7.56	2.82	−4.74
Mg–Fe	7.08	2.30	−4.78
Mg–Sr	8.40	3.34	−5.06
Mg–Ba	11.16	5.21	−5.95
Co–Fe	7.06	2.17	−4.89
Co–Sr	8.39	3.21	−5.18
Co–Ba	11.12	5.19	−5.96
Fe–Sr	7.82	2.72	−5.10
Fe–Ba	10.57	4.79	−5.78
Sr–Ba	11.91	5.73	−6.18

those calculated for Ni–Fe. Other dual dopants exhibit high solution energies. Solution energies for Ba containing dual dopants are highly endoergic, suggesting that they are unfavorable.

2. Trivalent dopants

The trivalent doping process in $CaMnO_3$ will lead to the formation of one oxygen vacancy per two trivalent dopants according to the following reaction equation:

$$M_2O_3 + 2Mn_{Mn}^{X} + O_o^{X} \rightarrow 2M'_{Mn} + V_O^{\bullet\bullet} + 2MnO_2. \quad (13)$$

As discussed earlier, solution energies were calculated in isolated and cluster forms [refer to Fig. 8(a)]. In all cases, solution energies calculated using isolated defects are higher than those calculated using defect clusters. The most stable dopant for this process is Al. However, Ga is calculated to be the most promising dopant if the defects are considered further apart. Solution energy increases with an increasing ionic radius. The highest solution energy is observed for La^{3+} because of its larger ionic radius. Binding energies are reported together with electronegativities in Fig. 8(b). In general,

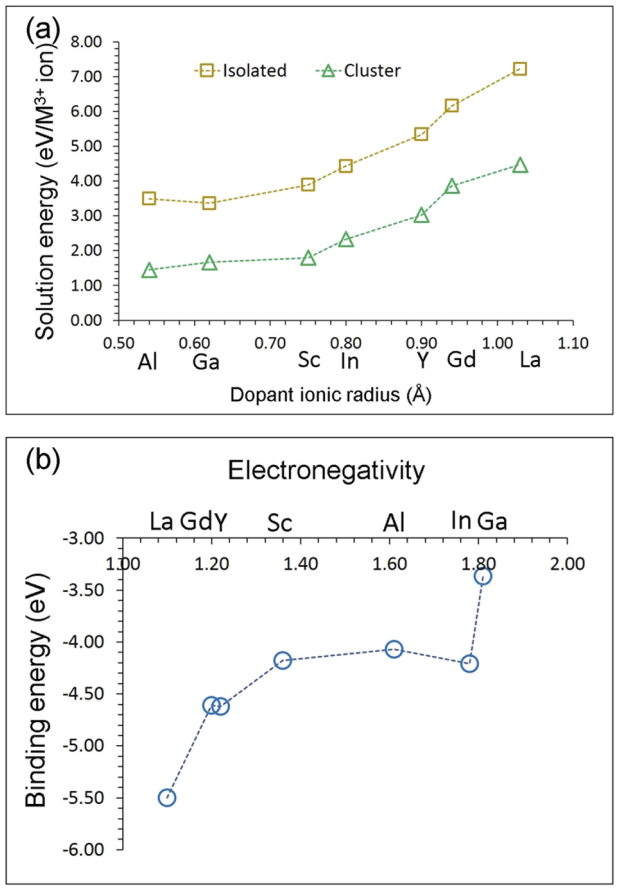

FIG. 8. (a) Solution energy of M_2O_3 (M = Al, Ga, Sc, In, Y, Gd, and La) with respect to the M^{3+} ionic radius and (b) binding energy of corresponding isolated defects forming a cluster with respect to electronegativity of the dopants.

there is a gradual increase in the binding energy with increasing electronegativity except for Y and In.

Dual trivalent dopants (M or R = Al, Ga, In, Sc, Y, Gd, and La) were considered next on the Mn sites. A single oxygen vacancy can be introduced in the lattice for every two dopants as described by the following equation:

$$\frac{1}{2}M_2O_3 + \frac{1}{2}R_2O_3 + 2Mn_{Mn}^{X} + O_o^{X} \rightarrow M'_{Mn} + R'_{Mn} + V_O^{\bullet\bullet} + 2MnO_2. \quad (14)$$

Table VII lists the solution energies of all combinations of dual dopants together with binding energies. The most favorable dual trivalent dopant is Al–Ga. Solution energies of Al–Sc, Ga–Sc, Al–In, Ga–In, and In–Sc are higher only by a maximum of 0.5 eV than that of Al–Ga. Other dual dopants exhibit high solution energies, and in particular, Gd–La is unlikely to dope at normal temperatures. In all cases, the binding energies are negative, confirming the aggregation of isolated defects to form clusters.

3. Tetravalent dopants

Finally, tetravalent cations (Si^{4+}, Ge^{4+}, Ti^{4+}, Sn^{4+}, Zr^{4+}, and Ge^{4+}) were considered on the Mn site. The following reaction equation was used to calculate the solution energy:

$$MO_2 + Mn_{Mn}^{X} \rightarrow M_{Mn}^{X} + MnO_2. \quad (15)$$

Figure 9 reports the solution energies. Exoergic solution energies are calculated for Ge^{4+} (−1.17 eV) and Si^{4+} (−0.18 eV). The preference of Ge^{4+} on the Mn site can be due to its ionic radius (0.53 Å) matching perfectly with the ionic radius of Mn^{4+}. Negative solution energy

TABLE VII. Solution energies calculated for dual-trivalent dopants substituted on the Mn site.

Co-dopants	Solution energy (eV/dopant)		Binding energy (eV)
	Isolated	Cluster	
Al–Ga	3.42	1.57	−1.85
Al–In	3.96	1.93	−2.03
Al–Sc	3.69	1.65	−2.03
Al–Y	4.42	2.30	−2.12
Al–Gd	4.82	2.72	−2.10
Al–La	5.36	3.02	−2.34
Ga–In	3.90	2.03	−1.87
Ga–Sc	3.62	1.75	−1.87
Ga–Y	4.35	2.43	−1.92
Ga–Gd	4.76	2.82	−1.94
Ga–La	5.29	3.12	−2.17
In–Sc	4.15	2.08	−2.07
In–Y	4.89	2.70	−2.19
In–Gd	5.30	3.12	−2.18
In–La	5.84	3.42	−2.42
Sc–Y	4.62	2.43	−2.19
Sc–Gd	5.02	2.84	−2.18
Sc–La	5.56	3.14	−2.42
Y–Gd	5.75	3.45	−2.30
Y–La	6.29	3.75	−2.54
Gd–La	5.75	4.16	−1.59

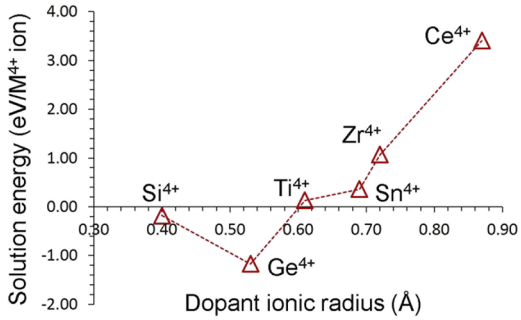

FIG. 9. Solution energy of MO_2 (M = Si, Ge, Ti, Sn, Zr, and Ce) with respect to the M^{4+} ionic radius.

calculated for Si^{4+} is due to its ionic radius (0.39 Å) being smaller than that of Mn^{4+}. Solution energy calculated for Ti^{4+} is slightly positive (0.13 eV), meaning that this dopant is also worth testing experimentally. Solution energy increases with the ionic radius from Sn^{4+} to Ce^{4+}. The highest solution energy (3.41 eV) is calculated for Ce^{4+}.

V. CONCLUSION

Atomistic simulation techniques were used to provide detailed insights into defect, diffusion, and dopant properties of $CaMnO_3$. The most favorable intrinsic defect is the anti-site defect; a small number of Ca^{2+} and Mn^{4+} ions exchange their atomic positions, leading to structural disorder. Systemic analysis of the ion-hopping mechanism shows that the diffusion of O^{2-} ions is faster than that of Ca^{2+} ions although activation energies of both ions are greater than 1 eV, implying poor ionic conductivity. The promising isovalent dopants on the Ca and Mn sites are predicted to be Fe^{2+} and Ge^{4+}, respectively. Subvalent doping of Fe^{2+} and Al^{3+} on the Mn site is a viable engineering strategy to increase the oxygen vacancies in this material. The most favorable dual divalent and trivalent dopants are calculated to be Ni–Fe and Al–Ga, respectively.

ACKNOWLEDGMENTS

The research leading to these results has received funding from the European Union's H2020 Programme under Grant Agreement No. 824072, HARVESTORE. Computational facilities and support were provided by the High Performance Computing Center at Imperial College London.

The authors declare that there is no competing financial interest.

DATA AVAILABILITY

The data that support the findings of this study are available from the corresponding author upon reasonable request.

REFERENCES

[1] M. A. Peña and J. L. G. Fierro, Chem. Rev. **101**, 1981 (2001).
[2] H. Wang, W. Su, J. Liu, and C. Wang, J. Materiomics **2**, 225 (2016).

[3]N. Labhasetwar, G. Saravanan, S. Kumar Megarajan, N. Manwar, R. Khobragade, P. Doggali, and F. Grasset, Sci. Technol. Adv. Mater. **16**, 036002 (2015).
[4]N. Ramadass, Mater. Sci. Eng. **36**, 231 (1978).
[5]W. Zhong, C.-T. Au, and Y.-W. Du, Chin. Phys. B **22**, 057501 (2013).
[6]H. He, Z. Yang, Y. Xu, A. T. Smith, G. Yang, and L. Sun, Nano Convergence **7**, 32 (2020).
[7]J. H. Park, Y. A. Lee, J. H. Yu, J. H. Lee, H. Yoon, Y. Cho, and C.-Y. Yoo, J. Asian Ceram. Soc. **8**, 519 (2020).
[8]Q. Guo, X. Li, H. Wei, Y. Liu, L. Li, X. Yang, X. Zhang, H. Liu, and Z. Lu, Front. Chem. **7**, 224 (2019).
[9]Q. Shen, S. Li, G. Yang, B. Sunden, and J. Yuan, Energies **12**, 410 (2019).
[10]Q. Ji, L. Bi, J. Zhang, H. Cao, and X. S. Zhao, Energy Environ. Sci. **13**, 1408 (2020).
[11]A. Chroneos, B. Yildiz, A. Tarancón, D. Parfitt, and J. A. Kilner, Energy Environ. Sci. **4**, 2774 (2011).
[12]E. N. Sgourou, Y. Panayiotatos, K. Davazoglou, A. L. Solovjov, R. V. Vovk, and A. Chroneos, Appl. Sci. **10**, 2286 (2020).
[13]X. Han, Y. Hu, J. Yang, F. Cheng, and J. Chen, Chem. Commun. **50**, 1497 (2014).
[14]J. Du, T. Zhang, F. Cheng, W. Chu, Z. Wu, and J. Chen, Inorg. Chem. **53**, 9106 (2014).
[15]M. Schrade, R. Kabir, S. Li, T. Norby, and T. G. Finstad, J. Appl. Phys. **115**, 103705 (2014).
[16]B. Fisher, L. Patlagan, G. M. Reisner, and A. Knizhnik, Phys. Rev. B **61**, 470 (2000).
[17]M. Molinari, D. A. Tompsett, S. C. Parker, F. Azough, and R. Freer, J. Mater. Chem. A **2**, 14109 (2014).
[18]Y. Wang, Y. Sui, H. Fan, X. Wang, Y. Su, W. Su, and X. Liu, Chem. Mater. **21**, 4653 (2009).
[19]D. S. Alfaruq, E. H. Otal, M. H. Aguirre, S. Populoh, and A. Weidenkaff, J. Mater. Res. **27**, 985 (2012).
[20]S. Peng, X. Han, L. Li, S. Chou, D. Ji, H. Huang, Y. Du, J. Liu, and S. Ramakrishna, Adv. Energy Mater. **8**, 1800612 (2018).
[21]A. Badreldin, A. E. Abusrafa, and A. Abdel-Wahab, Emergent Mater. **3**, 567 (2020).
[22]L. Chang, J. Li, Z. Le, P. Nie, Y. Guo, H. Wang, T. Xu, and X. Xue, J. Colloid Interface Sci. **584**, 698 (2021).
[23]R. Kabir, R. Tian, T. Zhang, R. Donelson, T. T. Tan, and S. Li, J. Alloys Compd. **628**, 347 (2015).
[24]J. F. Shin, H. Niu, J. Alaria, J. B. Claridge, and M. J. Rosseinsky, Phys. Chem. Chem. Phys. **19**, 30781 (2017).
[25]R. Kabir, T. Zhang, D. Wang, R. Donelson, R. Tian, T. T. Tan, and S. Li, J. Mater. Sci. **49**, 7522 (2014).
[26]D. Srivastava *et al.*, J. Mater. Chem. C **3**, 12245 (2015).
[27]G. V. Lewis and C. R. A. Catlow, J. Phys. C: Solid State Phys. **18**, 1149 (1985).
[28]M. Cherry, M. S. Islam, and C. R. A. Catlow, J. Solid State Chem. **118**, 125 (1995).
[29]R. W. Grimes, G. Busker, M. A. McCoy, A. Chroneos, J. A. Kilner, and S.-P. Chen, Ber. Bunsengesellschaft Phys. Chem. **101**, 1204 (1997).
[30]D. Rupasov, A. Chroneos, D. Parfitt, J. A. Kilner, R. W. Grimes, S. Y. Istomin, and E. V. Antipov, Phys. Rev. B **79**, 172102 (2009).
[31]C. A. J. Fisher, N. Kuganathan, and M. S. Islam, J. Mater. Chem. A **1**, 4207 (2013).
[32]R. Kaushalya, P. Iyngaran, N. Kuganathan, and A. Chroneos, Energies **12**, 3094 (2019).
[33]N. Kuganathan, P. Iyngaran, R. Vovk, and A. Chroneos, Sci. Rep. **9**, 4394 (2019).
[34]M. S. Islam, D. J. Driscoll, C. A. J. Fisher, and P. R. Slater, Chem. Mater. **17**, 5085 (2005).
[35]J. D. Gale and A. L. Rohl, Mol. Simul. **29**, 291 (2003).
[36]J. D. Gale, J. Chem. Soc., Faraday Trans. **93**, 629 (1997).
[37]N. F. Mott and M. J. Littleton, Trans. Faraday Soc. **34**, 485 (1938).
[38]N. Kuganathan, F. Baiutti, A. Tarancón, J. Fleig, and A. Chroneos, Solid State Ionics **361**, 115570 (2021).
[39]N. Kuganathan, M. J. D. Rushton, R. W. Grimes, J. A. Kilner, E. I. Gkanas, and A. Chroneos, Sci. Rep. **11**, 451 (2021).
[40]M. S. Islam and C. A. J. Fisher, Chem. Soc. Rev. **43**, 185 (2014).
[41]K. R. Poeppelmeier, M. E. Leonowicz, J. C. Scanlon, J. M. Longo, and W. B. Yelon, J. Solid State Chem. **45**, 71 (1982).
[42]C. Tealdi, M. Saiful Islam, L. Malavasi, and G. Flor, J. Solid State Chem. **177**, 4359 (2004).
[43]S. M. Woodley, C. R. A. Catlow, P. Piszora, K. Stempin, and E. Wolska, J. Solid State Chem. **153**, 310 (2000).
[44]P. M. Panchmatia, A. Orera, E. Kendrick, J. V. Hanna, M. E. Smith, P. R. Slater, and M. S. Islam, J. Mater. Chem. **20**, 2766 (2010).
[45]K. Alexopoulos and P. Varotsos, Phys. Rev. B **24**, 3606 (1981).
[46]P. A. Varotsos and K. D. Alexopoulos, in *Defects in Solids*, edited by S. Amelinckx (Elsevier, 1986), Vol. 14, p. 147.
[47]A. Chroneos and R. V. Vovk, Solid State Ionics **274**, 1 (2015).
[48]F. A. Kröger and H. J. Vink, in *Solid State Physics*, edited by F. Seitz and D. Turnbull (Academic Press, 1956), Vol. 3, p. 307.
[49]A. R. Armstrong, N. Kuganathan, M. S. Islam, and P. G. Bruce, J. Am. Chem. Soc. **133**, 13031 (2011).
[50]V. V. Politaev, A. A. Petrenko, V. B. Nalbandyan, B. S. Medvedev, and E. S. Shvetsova, J. Solid State Chem. **180**, 1045 (2007).
[51]M. Kempaiah Devaraju, Q. Duc Truong, H. Hyodo, Y. Sasaki, and I. Honma, Sci. Rep. **5**, 11041 (2015).
[52]A. Torres, F. J. Luque, J. Tortajada, and M. E. Arroyo-de Dompablo, Sci. Rep. **9**, 9644 (2019).
[53]N. Kuganathan and A. Chroneos, Energies **13**, 1285 (2020).
[54]A. Torres, F. J. Luque, J. Tortajada, and M. E. Arroyo-de Dompablo, Energy Storage Mater. **21**, 354 (2019).
[55]B. Bulfin *et al.*, J. Mater. Chem. A **5**, 7912 (2017).